

Multi-wavelength observations of the lensed quasar PKS 1830–211 during the 2019 γ -ray flare

S. Vercellone,^{1*} I. Donnarumma², C. Pittori^{3,4}, F. Capitanio⁵, A. De Rosa⁵, L. Di Gesu², S. Kiehlmann^{6,7}, M. N. Iacolina², P. A. Pellizzoni⁸, E. Egron⁸, L. Pacciani⁵, G. Piano⁵, S. Puccetti², S. Righini⁹, G. Valente², F. Verrecchia^{3,4}, V. Vittorini⁵, M. Tavani⁵, E. Brocato^{3,10}, A. W. Chen¹¹, T. Hovatta^{12,13}, A. Melis⁸, W. Max–Moerbeck¹⁴, D. Perrodin⁸, M. Pilia⁸, M. Pili⁸, A. C. S. Readhead¹⁵, R. Reeves¹⁶, A. Ridolfi⁸, F. Vitali³, A. Bulgarelli¹⁷, P. W. Cattaneo¹⁸, F. Lucarelli^{3,4}, A. Morselli¹⁹, A. Trois⁸

¹INAF, Osservatorio Astronomico di Brera, Via Emilio Bianchi 46, I-23807 Merate (LC), Italy

²ASI, Via del Politecnico, I-00133 Roma, Italy

³INAF, Osservatorio Astronomico di Roma, via Frascati 33, I-00078 Monte Porzio Catone, Italy

⁴ASI Space Science Data Center, Via del Politecnico, I-00133 Roma, Italy

⁵INAF, Istituto di Astrofisica e Planetologia Spaziali, Via Fosso del Cavaliere 100, I-00133 Roma, Italy

⁶Institute of Astrophysics, Foundation for Research and Technology-Hellas, GR-71110 Heraklion, Greece

⁷Department of Physics, Univ. of Crete, GR-70013 Heraklion, Greece

⁸INAF, Osservatorio Astronomico di Cagliari, Via della Scienza 5, I-09047 Selargius (CA), Italy

⁹INAF, Istituto di Radioastronomia, via Piero Gobetti 93/2, I-40129 Bologna, Italy

¹⁰INAF, Osservatorio Astronomico d'Abruzzo, Via Mentore Maggini, I-64100 Teramo, Italy

¹¹School of Physics, University of the Witwatersrand, 1 Jan Smuts Avenue, Braamfontein 2000 Johannesburg, South Africa

¹²Finnish Center for Astronomy with ESO (FINCA), University of Turku, FI-20014, Turku, Finland

¹³Aalto University Metsähovi Radio Observatory, Metsähovintie 114, 02540 Kylmälä, Finland

¹⁴Departamento de Astronomía, Universidad de Chile, Camino El Observatorio 1515, Las Condes, Santiago, Chile

¹⁵Owens Valley Radio Observatory, California Institute of Technology, Pasadena, CA 91125, USA

¹⁶Departamento de Astronomía, Universidad de Concepción, Concepción, Chile

¹⁷INAF, Osservatorio di Astrofisica e Scienza dello Spazio, via Gobetti 101, I-40129 Bologna (BO), Italy

¹⁸INFN Sezione di Pavia, via U. Bassi 6, I-27100 Pavia (PV), Italy

¹⁹INFN Sezione di Roma Tor Vergata, Via della Ricerca Scientifica 1, I-00133 Roma, Italy

Accepted XXX. Received YYY; in original form ZZZ

ABSTRACT

PKS 1830–211 is a γ -ray emitting, high-redshift ($z = 2.507 \pm 0.002$), lensed flat-spectrum radio quasar. During the period mid-February to mid-April 2019, this source underwent a series of strong γ -ray flares that were detected by both AGILE-GRID and *Fermi*-LAT, reaching a maximum γ -ray flux of $F_{E>100\text{MeV}} \approx 2.3 \times 10^{-5}$ photons $\text{cm}^{-2} \text{s}^{-1}$. Here we report on a coordinated campaign from both on-ground (Medicina, OVRO, REM, SRT) and orbiting facilities (AGILE, *Fermi*, INTEGRAL, *NuSTAR*, *Swift*, *Chandra*), with the aim of investigating the multi-wavelength properties of PKS 1830–211 through nearly simultaneous observations presented here for the first time. We find a possible break in the radio spectra in different epochs above 15 GHz, and a clear maximum of the 15 GHz data approximately 110 days after the γ -ray main activity periods. The spectral energy distribution shows a very pronounced Compton dominance (> 200) which challenges the canonical one-component emission model. Therefore we propose that the cooled electrons of the first component are re-accelerated to a second component by, e.g., kink or tearing instability during the γ -ray flaring periods. We also note that PKS 1830–211 could be a promising candidate for future observations with both Compton satellites (e.g., e-ASTROGAM) and Cherenkov arrays (CTAO) which will help, thanks to their improved sensitivity, in extending the data availability in energy bands currently uncovered.

Key words: acceleration of particles – radiation mechanisms: non-thermal – relativistic processes – quasars: super-massive black-holes – quasars: individual: PKS 1830–211 – gamma rays: galaxies

1 INTRODUCTION

PKS 1830–211 is a high-redshift blazar ($z = 2.507 \pm 0.002$;

Lidman et al. 1999) that is gravitationally lensed by a spiral galaxy at $z = 0.886$ (Wiklind & Combes 1996), as shown by the two radio lobes located 1" apart from each other (A e B components, Lovell et al. 1998). The lensed counterparts were also observed in the near-IR (NIR) and optical energy bands by the Hubble Space Telescope and

* E-mail: stefano.vercellone@inaf.it (SV)

the Gemini Observatory (Courbin et al. 2002). The source was observed in X-rays by both XMM-Newton and *Chandra*, enabling for a study of the complex soft X-ray behavior in detail (De Rosa et al. 2005; Dai et al. 2008). PKS 1830–211 is a well-known γ -ray source above 100 MeV, identified as such by Mattox et al. (1997) and subsequently listed in both the AGILE (Verrecchia et al. 2013; Bulgarelli et al. 2019) and *Fermi*-LAT (Abdollahi et al. 2020) catalogues, which has produced several γ -ray flares over the last two decades (Hartman et al. 1999; Donnarumma et al. 2011; Abdo et al. 2015). A quite bright γ -ray flare was detected by AGILE and *Fermi*-LAT in October–November 2010, and multi-wavelength observations were carried out, as reported in Donnarumma et al. (2011) and Abdo et al. (2015). The multi-wavelength campaign carried out in 2010 with AGILE (Donnarumma et al. 2011) showed that the intense γ -ray flare had no significant counterpart at lower frequencies, making this blazar classified as a “ γ -ray only flaring blazar”. This behaviour was discussed according to both (macro/micro) lensing and intrinsic physical properties of the blazar. In particular, macro and micro-lensing were excluded, given the chromaticity of the flare and the time scale of the γ -ray variability (Donnarumma et al. 2011). The flare was therefore associated with intrinsic variations of the jet emission, which are difficult to be interpreted in the one zone leptonic model (Ghisellini et al. 1985) given the high Compton dominance (i.e., the ratio of the peak of the Compton to the synchrotron peak luminosities) of the typical two-bump spectral energy distribution (SED) in flat-spectrum radio quasars. Alternative models have been invoked to overcome the limits of the one-zone leptonic models, such as the “mirror model” (Tavani et al. 2015; Vittorini et al. 2017) or the “jet-cloud interaction model” (Araudo et al. 2010; Vittorini et al. 2014). A long term γ -ray monitoring program represents an optimal tool to search for the time delay between the emissions of the two lensed images A and B as measured in the radio maps (26_{-5}^{+4} days; Lovell et al. 1998).

AGILE did not detect any delay between the lensed components during the γ -ray activity recorded in October–November 2010, which would infer a lack of delay if the flux ratio of the two components is ~ 1 , as observed in radio (no conclusion could be drawn if this value was below 1 due to the AGILE sensitivity). The missing evidence of an echo can be explained with a flux ratio of the two components not equal to 1 in γ -rays. The dependence on energy of the flux ratio of the two components can be explained by invoking micro-lensing effects (Blackburne et al. 2006; Donnarumma et al. 2011; Abdo et al. 2015). Further analyses of the γ -ray light curve with a larger sensitivity were performed by Abdo et al. (2015). By scanning a longer period (August 2008 - July 2011), two large γ -ray flares of PKS 1830–211 were detected by *Fermi*-LAT with no evidence for a delayed activity. Nevertheless, Abdo et al. (2015) were able to place a lower limit of ~ 6 on the flux ratio between the two lensed images. Barnacka et al. (2015), analysing *Fermi*-LAT data between August 2008 and January 2015 found a γ -ray time-delay consistent with the radio one, while Abhir et al. (2021), analysing a time period in 2019 similar to the one discussed in this paper, found no clear evidence of such a γ -ray time-delay.

In this paper, we present the multi-frequency campaign on PKS 1830–211 during the period mid-February to mid-April 2019 and involving measurements in the radio, near infra-red, optical, UV, X-ray and γ -ray energy bands. The paper is organised as follows. Section 2 reports on the different facilities involved in this observing campaign. In Section 3 we discuss our results, while in Appendices A–D we report the multi-wavelength observations. We adopt a Λ -cold dark matter (Λ -CDM) cosmology (Planck Collaboration et al. 2020) with the following parameters $H_0 = 67.7$, $\Omega_m = 0.31$, and $\Omega_\Lambda = 0.69$.

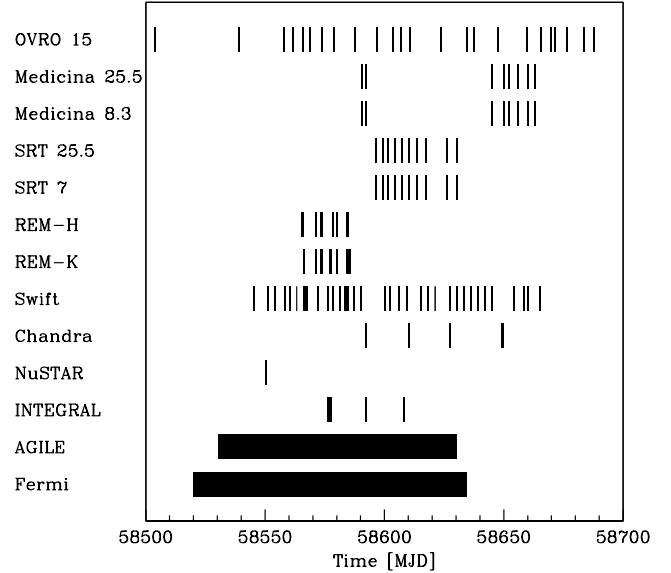


Figure 1. Coverage of the different facilities as a function of time. The first five values in the ordinate label refer to the observing frequency in GHz.

Table 1. List of facilities and their energy range.

Facility	Energy/ Wavelength/ Frequency
<i>Fermi</i> -LAT	0.1–300 GeV
AGILE-GRID	0.1–30 GeV
INTEGRAL-ISGRI	13–200 keV
<i>NuSTAR</i>	3–78.4 keV
<i>Chandra</i> -ACIS	0.5–8 keV
<i>Swift</i> -XRT	0.3–10 keV
<i>Swift</i> -UVOT	<i>v</i> 5468 Å <i>b</i> 4392 Å <i>u</i> 3465 Å <i>w1</i> 2600 Å <i>m2</i> 2246 Å <i>w2</i> 1928 Å
REM-REMIR	<i>K</i> 22000 Å
REM	<i>H</i> 16350 Å
SRT	<i>C-Band</i> 7 GHz <i>K-Band</i> 25.5 GHz
Medicina	<i>X-Band</i> 8.3 GHz <i>K-Band</i> 25.5 GHz
OVRO	15 GHz

2 SUMMARY OF OBSERVATIONS AND FLARE DEFINITION

The detection of γ -ray flares from PKS 1830–211 triggered a large multi-wavelength observing campaign, involving both on-ground (Medicina, OVRO, REM, SRT) and orbiting facilities (AGILE, *Fermi*, INTEGRAL, *NuSTAR*, *Swift*, *Chandra*).

Figure 1 shows the multi-wavelength coverage as a function of time of the different instruments, while Table 1 reports the differ-

Table 2. *Fermi*-LAT spectral properties during the different flaring periods.

Period	$F_{E>100\text{MeV}}$ (10^{-5} photons $\text{cm}^{-2} \text{s}^{-1}$)	α	β
F1	1.95 ± 0.07	2.44 ± 0.05	0.11 ± 0.03
F2	2.07 ± 0.07	2.26 ± 0.03	0.15 ± 0.02
F3	1.77 ± 0.07	2.33 ± 0.03	0.12 ± 0.02
4FGL	$(4.47 \pm 0.12) \times 10^{-2}$	2.46 ± 0.01	0.09 ± 0.01

ent energies covered by our campaign. These observations allow us to reconstruct an almost simultaneous spectral energy distribution spanning about fifteen decades in energy. The detailed description of each facility, data reduction, data analysis and the presentation of the results can be found in Appendix A (γ -ray data), Appendix B (X-ray data), Appendix C (IR, Optical, and UV data), and Appendix D (radio data). The *Fermi*-LAT 12-hr binning allows us to obtain a detailed description of the different γ -ray flares. We anticipate here the method we used for selecting the different γ -ray flares time-intervals.

“Unbinned light curves” were produced for the brightest flaring periods following the procedure described in Pacciani (2018), by means of a photometric method. Gamma-rays are collected within an extraction region of radius $R_{68\%}^i(E)$ that varies with the energy and type of the reconstructed γ -ray. $R_{68\%}^i(E)$ corresponds to the 68% containment radius of γ -rays of energy E and reconstruction topology PSF $_i$ (point-spread function, with $i = 1, \dots, 4$). A novel method to select flares within a set of time-tagged data has been used. It is a clustering method (iSRS, iterated short range search) in one dimension (the cumulative exposure domain), followed by a statistical discrimination based on maximum-score scan statistics (Glaz & Zhang 2006). Once the set of collected γ -rays are produced, a clustering scheme in the cumulative exposure domain is performed. Maximum-score scan statistics is applied to remove statistically not-relevant clusters (see Pacciani 2018, for details). The threshold chance probability to discriminate non-relevant clusters is set to 1.3‰. The set of remaining clusters is a root, with leaves corresponding to the detected peaks. Each cluster can be described by its mean time, the average flux within the cluster, and its length in time domain. In Figure 2 we show the set of remaining clusters (represented by a segment) for PKS 1830–211. We call this set the unbinned light curve. The most significant flares are F1 (MJD 58575.2–58576.1), F2 (MJD 58595.0–58598.8), and F3 (MJD 58601.5–58603.4). Table 2 shows the *Fermi*-LAT spectral properties during the different flaring periods, assuming a log-parabola model,

$$\frac{dN}{dE} = K_0 \left(\frac{E}{E_0} \right)^{-\alpha - \beta \ln(E/E_0)}, \quad (1)$$

where α is the spectral slope, β the curvature. The last value refers to the 4FGL Catalog one.

3 RESULTS AND DISCUSSION

3.1 Multi-wavelength data

Figure 3 shows the PKS 1830–211 multi-wavelength light-curves. From top to bottom we show the radio (OVRO 15 GHz, Medicina 8.3 GHz & 25.5 GHz, SRT 7 GHz & 25.5 GHz), IR (REM H-band and K-band), X-ray (*Swift*/XRT, *Chandra*), and γ -ray (AGILE-GRID and *Fermi*-LAT) data, respectively. The source reached its maximum flux ($F_{E>100\text{MeV}} = (2.28 \pm 0.25) \times 10^{-5}$ photons $\text{cm}^{-2} \text{s}^{-1}$) around April 24 (MJD= 58597.25 \pm 1.0), as shown in Panel (d). This flux

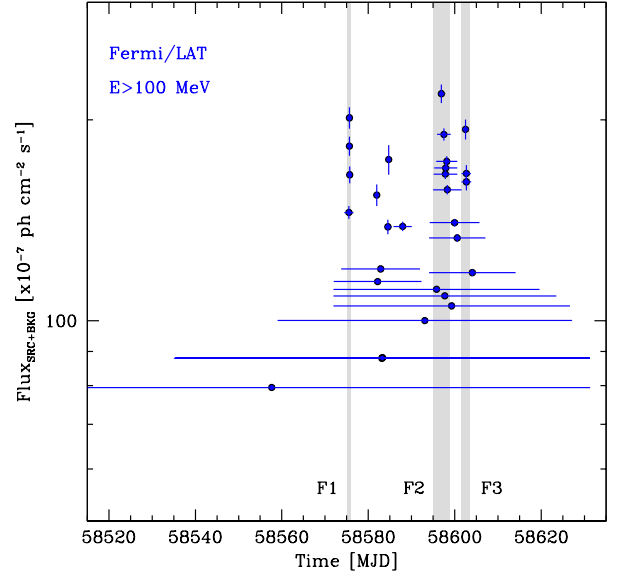


Figure 2. PKS 1830–211 *Fermi*-LAT unbinned light curve (a data clustering following Pacciani 2018). The most significant flares (and their durations) are reported as dashed areas. Background contribution is not subtracted. Dashed vertical bands correspond, from left to right, to F1, F2 and F3, respectively.

level is unprecedented for this source, and it is one of the largest ever detected in γ -rays from blazars at redshift $z > 2$ (see Vercellone et al. 2019, for 4C+71.07 at $z = 2.172$). Our *Chandra* data show that the flux is somewhat higher than what reported in De Rosa et al. (2005) for the *Chandra* observations of 2000-2001 and we also find an intervening column density $N_{\text{H,lens}}$ slightly higher than what found in De Rosa et al. (2005). To further investigate the possible variability of the spectral parameters of the source, we compared the count-rate observed in the two lensed images of PKS 1830–211 in a soft (0.5-2.0 keV) and in a hard (2.0-8.0 keV) energy band, as shown in Figure B2. In the last two shorter observations, the ratio is unconstrained in the soft band. A slight decrease of the ratio N/S is observed, in agreement with that reported in Wilms et al. (2019) for the ObsID 22197-22198. The decrease is more noticeable in the soft X-ray domain, which suggests variability of the absorbing column density in the lensing galaxy. However, higher quality, spatially resolved X-ray data would be needed to draw firm conclusions.

Figure 4 shows the OVRO 15 GHz light-curve starting from mid-October 2018 to mid-February 2020. The vertical grey bands marks the time-interval of the γ -ray flares. The light-curve shows the increasing trend of the 15 GHz flux during the γ -ray observations. This Figure clearly shows how the maximum of the 15 GHz emission occurs about 110 days after the major γ -ray activity period, followed by a decay ($\sim 4\text{Jy}$) in 100 days at a radio flux level comparable with the one at the onset of γ -ray flares. Pushkarev et al. (2010) found that there is a delay between the γ -ray and the radio emission (the γ -ray emission leads the radio one) up to eight months in the observer’s frame (an average of one month in the rest frame). According to Pushkarev et al. (2010), this evidence can be explained by the synchrotron opacity in the nuclear region. Our results, for $z = 2.507$, are perfectly in agreement with this scenario.

Figure 3, panel (a) shows the SRT/Medicina radio light-curve for

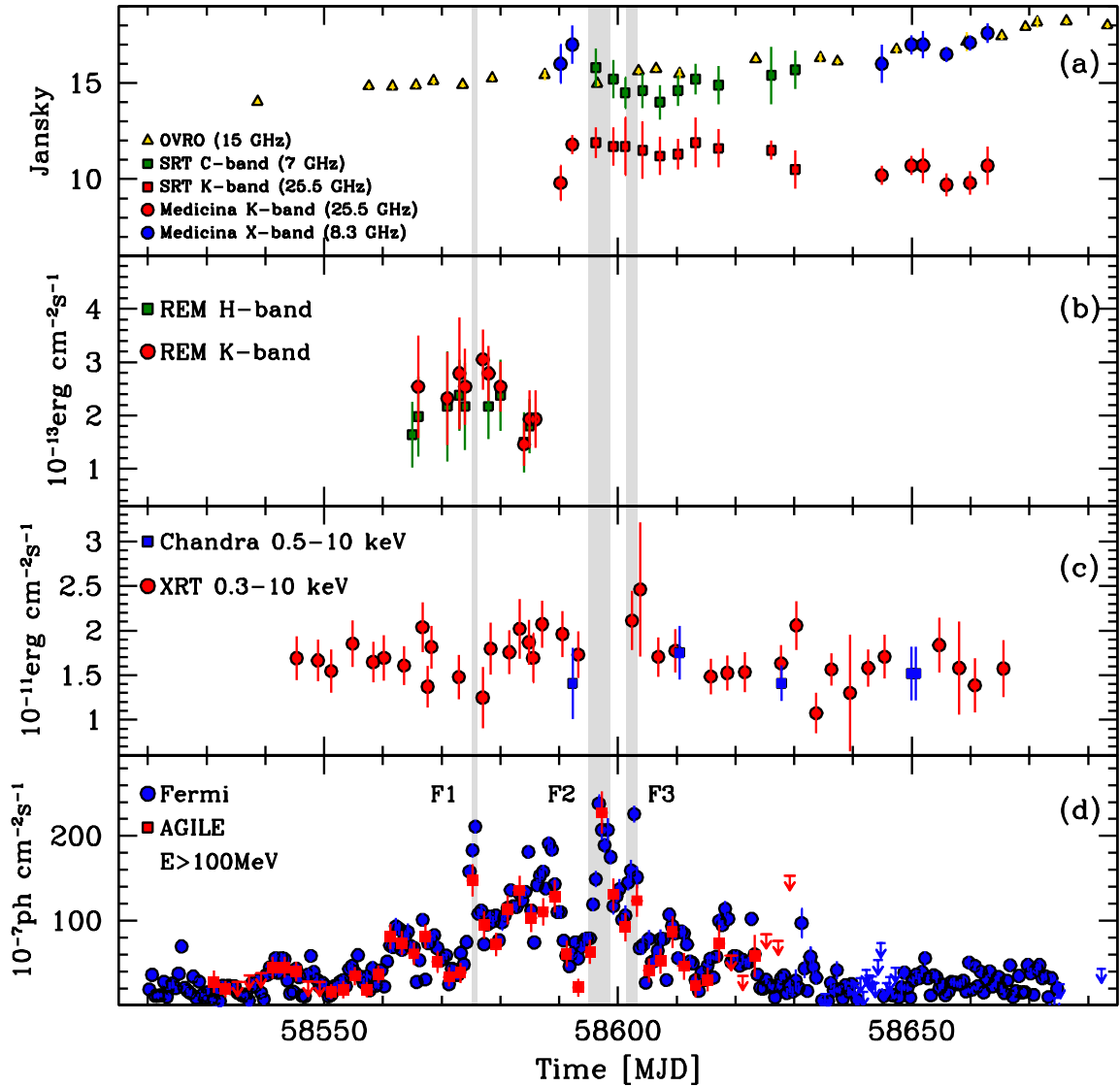


Figure 3. PKS 1830–211 multi-wavelength light-curves. From top to bottom: radio (7, 8.3, 15, 25.5) GHz, IR (H-band, K-band), X-ray (0.3–10) keV, and γ -ray ($E > 100$ MeV) data. The dashed areas correspond to the major γ -ray flares F1, F2 and F3, when the spectral energy distributions were computed. Arrows mark 3σ upper limits.

the 3 frequency bands observed: K-band (25.5 GHz) is indicated in red for both telescopes; X-band (8.3 GHz) in blue and C-band (7 GHz) in green. Data are reported in Table D1. The K-band light-curve displays a slight decrease in the observed time range, while lower frequency data seem to show a weak rise, although a clear trend is not evident and a short-term variability is detected. Therefore, a slight spectral break seems to manifest in the 56620–56640 MJD range. As the increasing flux density trend shown by OVRO data at 15 GHz has extended over about 58700 MJD (see Figure 4), the observed spectral break is likely to occur in the 15–26 GHz range. This break is clearly visible when analysing the SRT and Medicina radio spectra shown in Figure 5: a clear break emerges, with a decrease of the flux density

at the highest frequency in the observed time range. This is a typical behaviour observed during the course of a flare for extra-galactic jetted sources, which can undergo oscillations and variability of the radio flux density on week/month time scale, in a non-synchronous way at the several radio frequencies (see, e.g., Fromm et al. 2011).

Figure 6 shows the *Fermi*-LAT 12h-bin ($E > 300$ MeV) photon index as a function of the 12h-bin flux during the three main γ -ray flares F1, F2, and F3. It is worth noting that all the flares show the same achromatic behaviour, i.e., the photon index remains almost constant when the flux increases by a factor greater than 5. The average values of the γ -ray photon indices during the three different flares are $\Gamma_{F1} = 2.58 \pm 0.07$, $\Gamma_{F2} = 2.45 \pm 0.04$, and $\Gamma_{F3} = 2.50 \pm 0.06$.

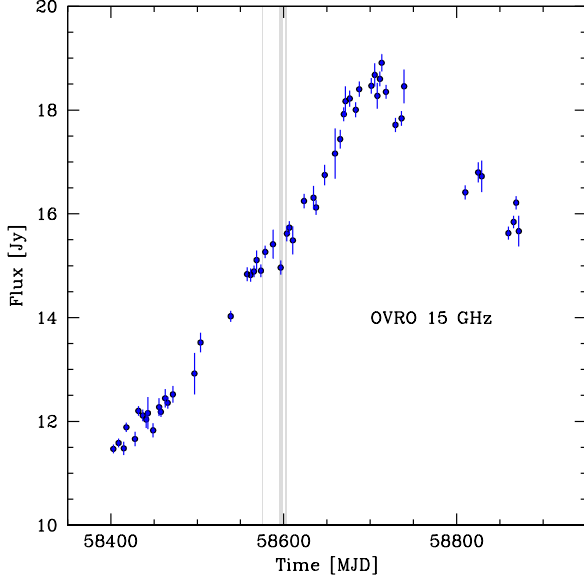


Figure 4. OVRO 15 GHz light-curve. The grey vertical bands mark the different γ -ray flares.

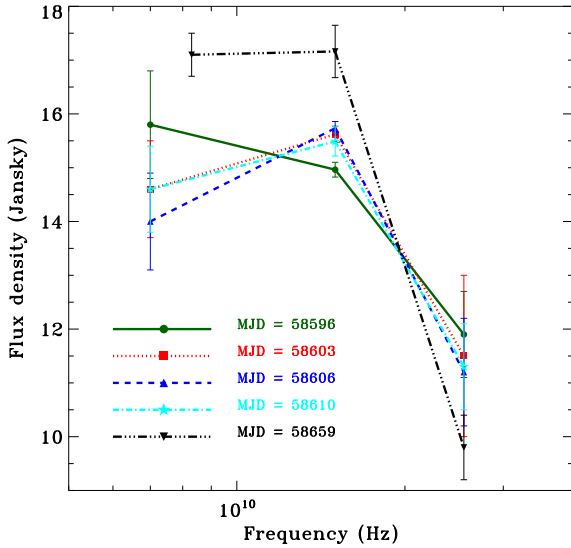


Figure 5. PKS 1830–211 radio spectra at different epochs. We include data from Medicina, OVRO and SRT telescopes at 7, 8.3, 15 and 25.5 GHz. The spectral points were integrated into period ranges whose MJD reference is indicated in the Figure.

These values are in agreement with the one reported in [Abdo et al. \(2010\)](#), $\Gamma = 2.46 \pm 0.18$, for FSRQs, as well as the low scatter as a function of the increasing flux. As noted by [Abdo et al. \(2010\)](#), the low dispersion observed may support the idea that a very limited number of physical parameters drive the spectrum shape in the GeV energy range and that it can also be connected to distinct dominant emission mechanisms, e.g. external Compton for FSRQs.

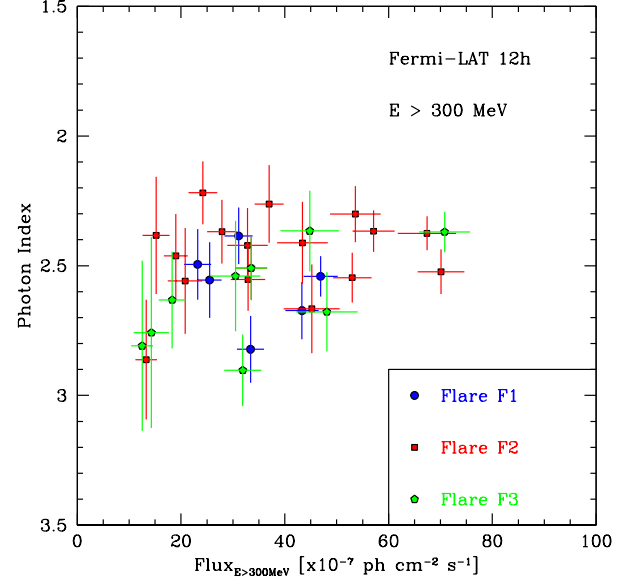


Figure 6. *Fermi*-LAT 12h-bin ($E > 300$ MeV) photon index as a function of the 12h-bin flux during the three main γ -ray flares F1, F2, and F3.

The 12-hour binning of the *Fermi*-LAT γ -ray light-curve allows us evaluate the fractional variability and its uncertainty,

$$F_{\text{var}} = \sqrt{\frac{S^2 - \bar{\sigma}^2}{\bar{x}^2}} \pm \sqrt{\left(\sqrt{\frac{1}{2N}} \frac{\bar{\sigma}_{\text{err}}}{\bar{x}^2 F_{\text{var}}}\right)^2 + \left(\sqrt{\frac{\bar{\sigma}_{\text{err}}^2}{N}} \frac{1}{\bar{x}}\right)^2} \quad (2)$$

according to formulae (10) and (B2) in [Vaughan et al. \(2003\)](#). We computed F_{var} for both $E > 100$ MeV $E > 300$ MeV in the period MJD 58520–58680, in order to check for any possible dependence of the variability on the energy threshold, obtaining $F_{\text{var}}^{E > 100 \text{ MeV}} = 0.842 \pm 0.007$ and $F_{\text{var}}^{E > 300 \text{ MeV}} = 0.723 \pm 0.015$, respectively. These results show a slightly enhanced variability when considering the lower energy threshold with respect to the higher one. We also computed F_{var} for the data at other frequencies. Only AGILE-GRID ($E > 100$ MeV), *Swift*-XRT (0.3–10 keV), and OVRO (15 GHz) data yield non-null F_{var} values: $F_{\text{var}}^{\text{AGILE}} = 0.62 \pm 0.04$, $F_{\text{var}}^{\text{XRT}} = 0.09 \pm 0.05$, and $F_{\text{var}}^{\text{OVRO}} = 0.078 \pm 0.003$, respectively. We note that, as seen in other blazars (e.g., 3C 454.3, [Vercellone et al. 2010](#)), F_{var} is higher in the γ -ray energy band than in the radio band. We should also consider that the calculation of F_{var} could be influenced both by the binning of the light-curve and by the source coverage at different frequencies, as discussed in detail in [Schleicher et al. \(2019\)](#).

We can also estimate the minimum variability time scale for $E > 100$ MeV by analysing the 12 hr-binned *Fermi*-LAT light-curve, $t_{\text{var}} = \ln(2) \times \tau_{\text{d}}$ days, where τ_{d} is the doubling(R, rising portion of the light-curve)/halving(D, decaying portion of the light-curve) time defined by

$$F(t_2) = F(t_1) \times 2^{(t_2 - t_1)/\tau_{\text{d}}}, \quad (3)$$

and $F(t_1)$ and $F(t_2)$ are the $E > 100$ MeV γ -ray fluxes at the times t_1 and t_2 , respectively. The AGILE-GRID γ -ray data have a much larger binning (48 hr) compared with the *Fermi*-LAT one (12 hr), which

Table 3. Minimum doubling (R, rising portion of the light-curve) and halving (D, decaying portion of the light-curve) time τ_d .

t_1 (MJD)	t_2 (MJD)	$F(t_1)$ (10^{-7} photons $\text{cm}^{-2} \text{s}^{-1}$)	$F(t_2)$ (10^{-7} photons $\text{cm}^{-2} \text{s}^{-1}$)	τ_d (Days)	Doubling/Halving Raise/Decay	Significance ($\sigma(\tau_d)$)
58539.75	58540.25	6.9 ± 1.9	36.0 ± 4.6	0.21	R	15.3
58527.75	58528.25	34.0 ± 4.6	8.2 ± 1.9	0.25	D	5.6

makes the AGILE data less constraining to assess time variability on short timescales. Table 3 shows the minimum doubling/halving times and their significance, $\sigma(\tau_d) = |F(t_1) - F(t_2)|/\sigma(F(t_1))$. We selected those doubling/halving times with $\sigma(\tau_d) \geq 3$. Assuming $\tau_d = \min\{\tau_d(R); \tau_d(D)\}$, we obtain the minimum variability timescale $t_{\text{var}} = 0.15$ days.

This quantity can be used to derive the minimum Doppler factor (Dondi & Ghisellini 1995),

$$\delta_{\min} \geq \left[3.5 \times 10^3 \frac{(1+z)^{2\alpha} (1+z - \sqrt{1+z})^2 F_x (3.8\nu_\gamma \nu_x)^\alpha}{t_{\text{var}}} \right]^{1/(4+2\alpha)} \quad (4)$$

where z is the source redshift, α is the energy spectral index in the X-ray band, F_x is the X-ray flux at 1 keV in μJy , ν_γ is the average energy of the maximum energy bin in GeV of the γ -ray spectrum, and ν_x is 1 keV. In order to derive the X-ray flux and spectral properties, we stacked all the *Swift*/XRT observations, because of their moderate variability. We obtain $F_{0.3-10\text{keV}} = (1.65^{+0.04}_{-0.04}) \times 10^{-11} \text{ erg cm}^{-2} \text{ s}^{-1}$ and $\alpha = 1.32^{+0.06}_{-0.05}$, which yields $\delta_{\min} \geq 24.3$.

3.2 Spectral energy distribution

During our observing campaign we collected multi-wavelength data covering the main γ -ray flares. Figure 7 shows the PKS 1830–211 spectral energy distribution (SED). In the radio and IR energy bands, points and colours follow those presented in Figure 3. Purple upper limits represent the *Swift*/UVOT data, integrated during the whole observing campaign. In the X-ray energy band, cyan and red points represent *Swift*/XRT spectra accumulated on MJD 58568–58578 (γ -ray F1) and MJD 58590–58606 (γ -ray F2+F3), respectively. Blue points represent *NuSTAR* data acquired on MJD 58550, while golden points are the sum of all the INTEGRAL/IBIS observations. The combined X-ray spectral model fitting was performed with the following parameters: $\text{const} * \text{phabs} * (\text{zphabs} * \text{pow})$ fixing the absorption along the line-of-sight to $N_{\text{H}}^{\text{gal}} = 0.187 \times 10^{22} \text{ cm}^{-2}$ and $N_{\text{H}}^{\text{lens}} = 3.1 \times 10^{22} \text{ cm}^{-2}$ (assuming $z_{\text{lens}} = 0.89$). Both fits yield a photon index of 1.46 ± 0.01 .

In the γ -ray energy band we investigated the *Fermi*-LAT finer time-binning in order to select the most significant flare episodes, F1, F2 and F3. The corresponding AGILE-GRID photon indices are $\Gamma(\text{F1}) = 2.35 \pm 0.14$, $\Gamma(\text{F2}) = 2.29 \pm 0.09$, and $\Gamma(\text{F3}) = 2.00 \pm 0.16$, respectively. Small grey points are archival data provided by the ASI/SSDC *SED Builder Tool* (Stratta et al. 2011) which include public catalogs and surveys. The data show the typical double-humped shape of the blazar SED. Moreover, while the rising branch of the inverse Compton and the poorly constrained synchrotron emission are almost consistent with the previous SEDs, the high-energy peak ($E > 100 \text{ MeV}$) is about a factor of 3–4 more intense with respect to the flare discussed in Donnarumma et al. (2011), whose SED fits are reported as dotted line (quiescent state), dashed line (one-month integration around the 2010 flare) and dot-dashed line (5-day flare).

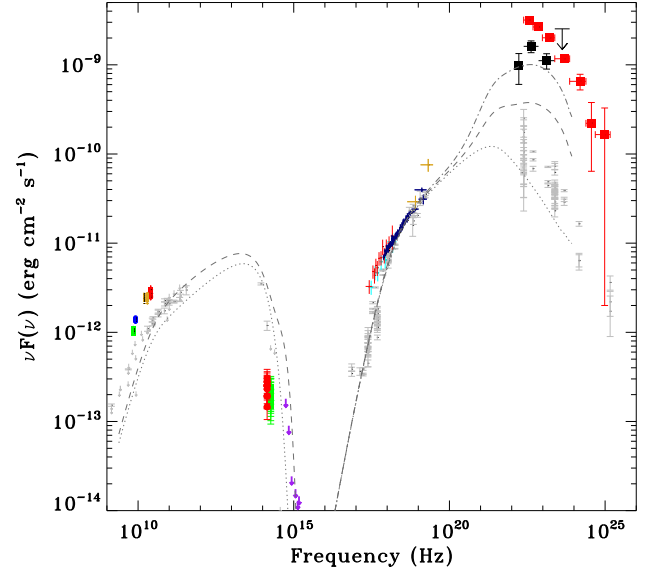


Figure 7. PKS 1830–211 spectral energy distributions for the three major γ -ray flares (see Section 3.2 for details). In the radio band, green, blue, golden and red points represent 7 GHz, 8.3 GHz, 15 GHz, and 25.5 GHz data. In the IR band, green and red points represent REM-H and REM-K bands, respectively. Purple upper limits represent the *Swift*/UVOT data, integrated during the whole observing campaign. In the X-ray energy band, cyan and red points represent *Swift*/XRT spectra accumulated on MJD 58568–58578 (γ -ray F1) and MJD 58590–58606 (γ -ray F2+F3), respectively. Blue points represent *NuSTAR* data acquired on MJD 58550, while golden points are the sum of all the INTEGRAL/IBIS observations. For sake of clarity, in the γ -ray energy band we report data pertaining to flare F1. Red filled squares correspond to *Fermi*-LAT F1 data, while black filled squares correspond to AGILE-GRID data acquired on a similar period. Small grey points are archival data. The dotted, dashed and dot-dashed dark-grey lines correspond to the 2010 SEDs for the average γ -ray state, the 1-month integration, and the 5-day γ -ray flare, respectively, as described in Donnarumma et al. (2011).

We model the flare F1 for which we have simultaneous data in radio, IR, optical, X-ray and γ -ray bands (IR data are relevant to constrain the synchrotron component). The data show very high Compton dominance, with stronger daily variability in γ -rays than the others bands: these data challenge a simple one-zone model (see e.g., Vittorini et al. 2017). Adapting the original model discussed in Vittorini et al. (2009), we first consider the emission in optical-UV. Assuming a magnification factor due to gravitational lensing of the order of 10 (see e.g. Donnarumma et al. 2011), the accretion disk has to radiate $L_d \lesssim 10^{45} \text{ erg s}^{-1}$ at black-body temperature $T_d \approx 3 \times 10^4 \text{ K}$, while the broad-line region (BLR) reprocesses 5% of this radiation from a radius $R_{\text{BLR}} \approx 0.05 \text{ pc}$, typical for these disc luminosities. We also consider a dusty torus having extension $R_{\text{Torus}} \approx 1 \text{ pc}$ that emits infrared photons at black-body temperature

Table 4. Model parameters for the AGN.

Ext. source	$L(10^{45} \text{ erg s}^{-1})$	$T(\text{K})$	$R(\text{pc})$
<i>Accr. disk</i>	1	3×10^4	$R_{\text{BLR}} = 0.05$
<i>Dusty torus</i>	1	100	$R_{\text{Torus}} = 1$

Table 5. Model parameters for the γ -ray flare F1.

Comp.	θ	$B(\text{G})$	γ_b	ζ_1	ζ_2	γ_{max}
<i>cI</i>	1.5	1	600	2.3	3.5	10^3
<i>cII</i>	1	0.2	500	2.1	3.5	3×10^3

$T_{\text{Torus}} \approx 100 \text{ K}$ with luminosity $L_{\text{T}} \approx L_{\text{d}}$. Therefore, we consider an internal electron population *cI* in a jet region of longitudinal size $L \approx 10^{17} \text{ cm}$ and tangled magnetic field $B \approx 1 \text{ Gauss}$, moving with bulk Lorentz factor $\Gamma \approx 18$ (see, e.g., Tavecchio et al. 1998), in which the emission is due to synchrotron process and inverse Compton with the same synchrotron photons plus external photons coming from the accretion disk, the BLR and the dusty torus. At the BLR edge we assume that the cooled electrons of *cI* are re-accelerated to a *cII* component (of size $R \approx 3 \times 10^{16} \text{ cm}$) by, e.g., kink or tearing instability (Bodo et al. 2022) that slightly modifies the viewing angle θ . This second component accounts for the enhanced γ -ray flux via inverse Compton with the external soft photons. The magnetic field in *cII* is then assumed to decrease to 0.2 Gauss as the plasmoid moves away from the center, towards the BLR edge. Moreover, we assume the emitters to have a jet-frame distribution of the random energies (γmc^2), starting from $\gamma_{\text{min}} = 30$ (see, e.g., Donnarumma et al. 2011), in the form of a standard broken power-law

$$n_e(\gamma) = \frac{K \gamma_b^{-1}}{(\gamma/\gamma_b)^{\zeta_1} + (\gamma/\gamma_b)^{\zeta_2}}, \quad (5)$$

where ζ_1 and ζ_2 are the spectral indices for $\gamma < \gamma_b$ and $\gamma > \gamma_b$, respectively, γ_b is the Lorentz factor at the break and the normalisation is assumed $K \approx 1$ corresponding to an electron density $\sim 70 \text{ cm}^{-3}$ for *cI* and $K \approx 30$ corresponding to an electron density $\sim 10^3 \text{ cm}^{-3}$ for *cII*, respectively. Table 4 shows the parameters we assumed for PKS 1830–211, while Table 5 shows the values of the parameters for the two components, *cI* and *cII*, responsible for the overall SED. Assuming a bulk Lorentz factor $\Gamma \approx 18$ and the values of the viewing angles θ reported in Table 5, we obtain Doppler factors of the order of 29–32 for *cI* and *cII*, respectively. These values are in agreement with the minimum Doppler factor derived in Section 3.1.

Figure 8 shows the multi-component fit to our data, as described above. The different lines represent different emission components. We note that the main contribution to the IC peak is provided by the inverse Compton off the BLR photons, as suggested by the achromatic behaviour reported in Figure 6.

The Eddington luminosity is $L_{\text{Edd}} \approx 6.2 \times 10^{46} \text{ erg s}^{-1}$, where we assumed the value of the black hole mass reported by Nair et al. (2005), $M_{\text{BH}} = 5 \times 10^8 M_{\odot}$. The total power carried in the jet, P_{jet} , can be calculated following Ghisellini & Celotti (2001) as

$$P_{\text{jet}} = P_{\text{B}} + P_{\text{p}} + P_{\text{e}} + P_{\text{rad}}, \quad (6)$$

where P_{B} , P_{p} , P_{e} , and $P_{\text{rad}}^{\text{bol}}$ are the power carried by the magnetic field, the cold protons, the relativistic electrons, and the produced radiation, respectively. In order to compute the different com-

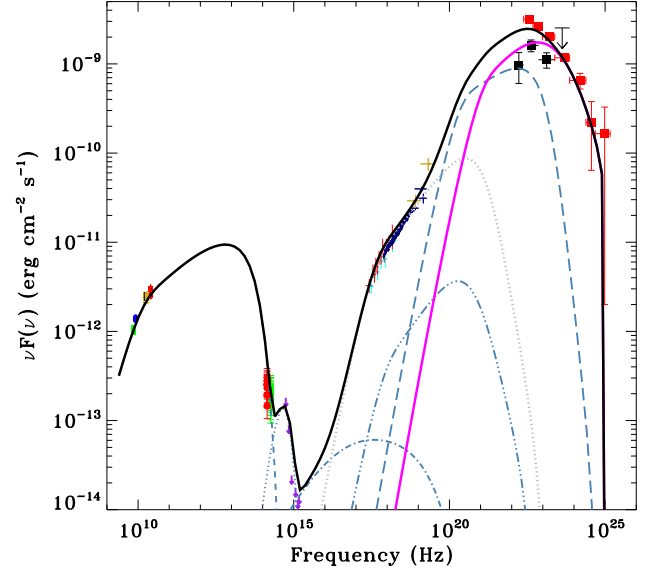


Figure 8. PKS 1830–211 spectral energy distributions for the flare F1 with different fit components. Data points follow the color scheme adopted for Figure 7. Different lines correspond to different spectral components. Blue-dotted is the disk emission, blue-dashed is the synchrotron emission, blue-dashed-dotted is the synchrotron self-Compton emission, blue-triple-dotted-dashed is external Compton off the disk photons emission, blue-long-dashed is the external Compton off the BLR photons emission, grey-dotted is the external Compton off the torus photons emission, magenta-solid is the external Compton off the BLR photons emission of component *cII*, and black-solid is the sum of all the different components.

ponents, we use the formalism presented in Celotti & Ghisellini (2008). We obtain: $P_{\text{B}} \approx 8 \times 10^{45} \text{ erg s}^{-1}$, $P_{\text{e}} \approx 5 \times 10^{44} \text{ erg s}^{-1}$, $P_{\text{p}} \approx 2 \times 10^{46} \text{ erg s}^{-1}$, $P_{\text{rad}} \approx 2.0 \times 10^{46} \text{ erg s}^{-1}$, which yields $P_{\text{jet}} \approx 5 \times 10^{46} \text{ erg s}^{-1}$. This is comparable to the maximum P_{jet} value computed during the October 2010 flare in Donnarumma et al. (2011). We also note that, due to the high variability of PKS 1830–211, the comparison of model parameters are not always straightforward. While the γ -ray flare modelled in Donnarumma et al. (2011) is not dramatically different from the one discussed in this work, the SED discussed in De Rosa et al. (2005) reached a γ -ray peak more than two order of magnitude lower than the present one, since they reported the Third EGRET Catalogue (Hartman et al. 1999) spectrum. We also note that, despite a different definition of the different γ -ray flares and SED model parameters, our P_{jet} estimate is compatible with the one reported in Abhir et al. (2021).

3.3 Prospects for detection in the MeV and VHE bands

Figure 9 shows the inverse Compton peak region of PKS 1830–211 data. The cyan curve represents the ASTROGAM sensitivity for an integration time of 6 days (see Vercellone et al. 2019, for further details). ASTROGAM is a proposed Observatory space mission dedicated to the study of the non-thermal Universe in the photon energy range from 0.3 MeV to 3 GeV (De Angelis et al. 2017, 2021). ASTROGAM could be a very useful mission in order to study high-redshift, powerful FS-RQs such as PKS 1830–211 (Donnarumma et al. 2011, and this work), 4C +71.07 (Vercellone et al. 2019) and a small sample

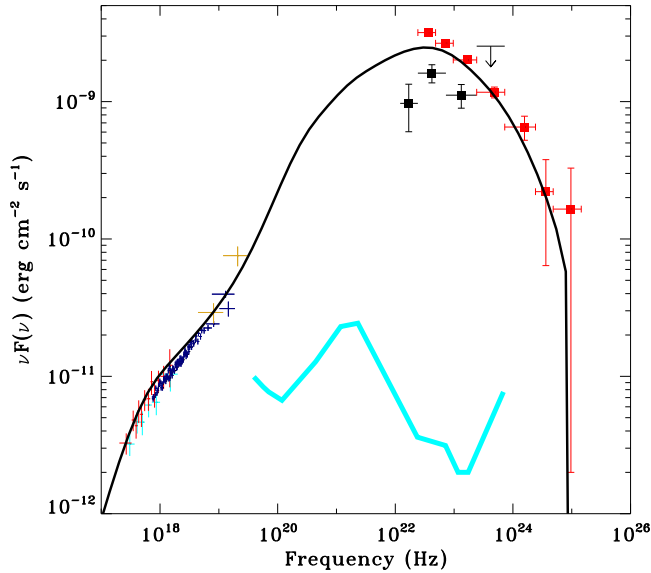


Figure 9. Inverse Compton peak region of PKS 1830–211. Data points and the black-solid line follow the color scheme adopted for Figure 7. The cyan curve represents the ASTROGAM sensitivity for an integration time of 6 days.

in Marcotulli et al. (2020). As seen in Figure 9, ASTROGAM would sample the IC component, providing crucial data which cover the energy range from 0.1 MeV up to a few hundreds of MeV. This would allow us to cover a currently unsampled energy range, and to obtain important data to constrain the IC peak in high- z FSRQs.

Figure 10 shows the *Fermi*-LAT data and power-law spectrum during flare F1, extrapolated to higher energies, in the optimistic assumption that no intrinsic cut-off applies. The correction for absorption by the extra-galactic background light (EBL), providing substantial attenuation only above a few tens of GeV, has been applied using the model of Domínguez et al. (2011, black solid line). We note that during a previous PKS 1830–211 γ -ray flare that occurred on 2014 July 27 (Krauss et al. 2014), the source was also observed by the H.E.S.S.-II array, starting about 20 days after the *Fermi*-LAT alert in order to investigate possible delayed emission at very high energies (H. E. S. S. Collaboration et al. 2019). This observation was performed by adding the large CT5 telescope, which provides detection capabilities below 100 GeV (H. E. S. S. Collaboration et al. 2017). No significant signal was detected above ~ 67 GeV. The green, gold, and blue solid lines correspond to the MAGIC (50 hr), H.E.S.S. (50 hr), and CTAO alpha configuration¹ (50, 5, and 0.5 hr) differential sensitivity, respectively. MAGIC can observe PKS 1830–211 at a Zenith angle of about 50 deg, which increases its low energy threshold, while the H.E.S.S.-I sensitivity (when considering the usual CT1–4 configuration) does not extend significantly at energies lower than 100 GeV. CTAO, in its alpha configuration, might be able to detect PKS 1830–211 with a short integration time (0.5–5) hr up to 100 GeV. The detection of FSRQs by IACTs may challenge

¹ The “Alpha Configuration” for the southern CTAO array consists of 14 medium-sized telescopes and 37 small-sized telescopes. See <https://www.cta-observatory.org/science/ctao-performance/> for further details.

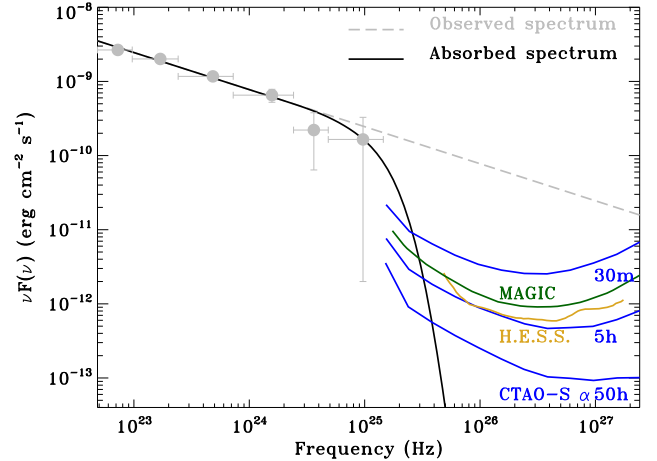


Figure 10. Grey data and dashed line represent the *Fermi*-LAT data and power-law spectrum during flare F1, while the black solid line represent the EBL-absorbed PKS 1830–211 spectrum at energies above 10 GeV. Green and golden lines represent the MAGIC and H.E.S.S.-I differential sensitivity curves for an integration time of 50 hr, respectively. Blue lines represent the CTAO-S Alpha Configuration differential sensitivity curves for different integration times (0.5, 5 and 50) hr (See <https://www.cta-observatory.org/science/ctao-performance/>).

the current paradigm of the HE-VHE emission occurring within or at the edge of the BLR. As shown in Costamante et al. (2018), the γ -ray emission from *Fermi*-LAT FSRQs might be explained by means of emitting mechanisms which do not involve the jet interaction with the BLR. Moreover, evidence is emerging that for blazars the location of the γ -ray emitting region may not always be placed at the same distance from the central black-hole during different flaring episodes of the same source as suggested by Brown (2013) for PKS 1510–089 or by Coogan et al. (2016) and Finke (2016) for 3C 454.3. A few FSRQs have been already detected by current IACTs (see also <http://tevcat.uchicago.edu/>). Therefore, the detection of PKS 1830–211 by CTAO during particular strong flares could shed light on the location of the gamma-ray emitting zone and the related emission mechanisms.

4 SUMMARY AND CONCLUSIONS

In this paper we presented the multi-wavelength behaviour, from radio frequencies up to the γ -ray energy band, of the lensed quasar PKS 1830–211 during multiple flaring episodes that occurred in the period mid-February to mid-April 2019 through nearly simultaneous observations presented here for the first time. We can summarise our findings as follows:

- (i) The *Fermi*-LAT data show three major γ -ray flares, F1 (MJD 58575.2–58576.1), F2 (MJD 58595.0–58598.8), and F3 (MJD 58601.5–58603.4), respectively. The minimum variability timescale for $E > 100$ MeV is $t_{\text{var}} = 0.15$ days, while it emerges there could be a slightly enhanced fractional variability when considering the lower energy threshold ($E > 100$ MeV) with respect to the higher one ($E > 300$ MeV). Moreover, we confirm the higher fractional variability in the γ -ray energy band with respect to the one at lower frequencies. Another interesting result is on γ -ray spectral variability as a function of the flux. As already noted for other sources (3C 454.3,

Vercellone & Romano 2014, in the 0.2-10 keV energy band) there is a roughly achromatic increase of the γ -ray emission. This could be explained, for example, with the dominance of the external Compton emission mechanism in the γ -ray energy band.

(ii) X-ray data show moderate variability during the whole observing period. A detailed analysis of *Chandra* data show a hint of variability of the absorbing column density in the lensing galaxy.

(iii) Radio data show an interesting behaviour. Investigating the data in the frequency range 7–25.5 GHz we find a spectral break above 15 GHz, with a decrease of the flux density at the highest frequency in the observed time range. Similar breaks in the radio spectra could be found in other extra-galactic jetted sources, due to radio flux variability at different wavelengths in times. Moreover, 15 GHz data show a continuous flux rising up to a maximum occurring about 110 days after the γ -ray flares, suggesting possible different locations of the γ -ray and radio emission zones.

(iv) UV-optical data are challenging to be acquired. While we have only upper-limits in the UV-optical wavebands, infra-red data show no particular variability pre-, during, and post-flare F1 episode.

(v) The SED modelling shows that our data are consistent with a multiple-component emission model, where the emission in the energy band above 100 MeV could be interpreted by the inverse Compton emission, at the edge of the BLR, of electrons re-accelerated by kink or tearing instability. Moreover, the total jet power is comparable to that of the 2010 flare.

(vi) Finally, PKS 1830–211 is an excellent candidate for upcoming both Compton and VHE facilities. Upcoming Compton missions will probe the IC peak in high-*z* FSRQs while a possible detection of PKS 1830–211 would increase the number of FSRQs detected at VHE and provide useful information of the location of the γ -ray emitting zone during different flares.

ACKNOWLEDGEMENTS

S.V., I.D., C.P., F.C., A.dR., L.dG., S.K., M.N.I., A.P.P., E.E., L.P., G.P., S.P., S.R., G.V., F.V., V.V. contributed equally to this work. We thank the referee for the prompt reply and the valuable comments which improved the quality of the manuscript. The authors acknowledge financial contribution from the grant ASI I/028/12/0. SV acknowledges financial contribution from the agreement ASI-INAf n.2017-14-H.0. The Sardinia Radio Telescope is funded by the Ministry of University and Research (MIUR), Italian Space Agency (ASI), and the Autonomous Region of Sardinia (RAS) and is operated as National Facility by the National Institute for Astrophysics (INAF). The Medicina radio telescope is funded by the Ministry of University and Research (MIUR) and is operated as National Facility by the National Institute for Astrophysics (INAF). This research has made use of data from the OVRO 40-m monitoring program (Richards et al. 2011), supported by private funding from the California Institute of Technology and the Max Planck Institute for Radio Astronomy, and by NASA grants NNX08AW31G, NNX11A043G, and NNX14AQ89G and NSF grants AST-0808050 and AST-1109911. S.K. acknowledges support from the European Research Council (ERC) under the European Unions Horizon 2020 research and innovation programme under grant agreement No. 771282. Part of this work is based on archival data, software or online services provided by the Space Science Data Center – ASI.

DATA AVAILABILITY

The data underlying this article are publicly available from the *Fermi*-LAT, AGILE-GRID, INTEGRAL, *NuSTAR*, *Chandra*, *Swift*, SRT/Medicina, and REM archives and processed with publicly available software (SRT/Medicina SDI software can be available upon request). OVRO 40-m data are available upon request to Sebastian Kiehlmann (skiehl@physics.uoc.gr).

REFERENCES

- Abdo A. A., et al., 2010, *ApJ*, **710**, 1271
 Abdo A. A., et al., 2015, *ApJ*, **799**, 143
 Abdollahi S., et al., 2020, *ApJS*, **247**, 33
 Abhir J., Prince R., Joseph J., Bose D., Gupta N., 2021, *ApJ*, **915**, 26
 Angioni R., 2019, The Astronomer’s Telegram, 12601
 Araudo A. T., Bosch-Ramon V., Romero G. E., 2010, *A&A*, **522**, A97
 Atwood W. B., et al., 2009, *ApJ*, **697**, 1071
 Baars J. W. M., Genzel R., Pauliny-Toth I. I. K., Witzel A., 1977, *A&A*, **500**, 135
 Barnacka A., Geller M. J., Dell’Antonio I. P., Benbow W., 2015, *ApJ*, **809**, 100
 Blackburne J. A., Pooley D., Rappaport S., 2006, *ApJ*, **640**, 569
 Bodo G., Mamatsashvili G., Rossi P., Mignone A., 2022, *MNRAS*, **510**, 2391
 Breeveld A. A., Landsman W., Holland S. T., et al. 2011, AIPC, 1358, 373
 Brown A. M., 2013, *MNRAS*, **431**, 824
 Bulgarelli A., Chen A. W., Tavani M., Gianotti F., Trifoglio M., Contessi T., 2012, *A&A*, **540**, A79
 Bulgarelli A., et al., 2014, *ApJ*, **781**, 19
 Bulgarelli A., et al., 2019, *A&A*, **627**, A13
 Burrows D. N., et al., 2005, *Space Sci. Rev.*, **120**, 165
 Cardillo M., et al., 2019, The Astronomer’s Telegram, 12622
 Celotti A., Ghisellini G., 2008, *MNRAS*, **385**, 283
 Coogan R. T., Brown A. M., Chadwick P. M., 2016, *MNRAS*, **458**, 354
 Costamante L., Cutini S., Tosti G., Antolini E., Tramacere A., 2018, *MNRAS*, **477**, 4749
 Courbin F., Meylan G., Kneib J.-P., Lidman C., 2002, *ApJ*, **575**, 95
 Dai X., Mathur S., Chartas G., Nair S., Garmire G. P., 2008, *AJ*, **135**, 333
 De Angelis A., et al., 2017, *Experimental Astronomy*, **44**, 25
 De Angelis A., et al., 2021, *Experimental Astronomy*, **51**, 1225
 De Rosa A., et al., 2005, *A&A*, **438**, 121
 Dickey J. M., Lockman F. J., 1990, *ARA&A*, **28**, 215
 Domínguez A., et al., 2011, *MNRAS*, **410**, 2556
 Dondi L., Ghisellini G., 1995, *MNRAS*, **273**, 583
 Donnarumma I., et al., 2011, *ApJ*, **736**, L30
 Egron E., et al., 2017a, *MNRAS*, **470**, 1329
 Egron E., et al., 2017b, *MNRAS*, **471**, 2703
 Feroci M., et al., 2007, *Nuclear Instruments and Methods in Physics Research A*, **581**, 728
 Finke J. D., 2016, *ApJ*, **830**, 94
 Fitzpatrick E. L., 1999, *PASP*, **111**, 63
 Fromm C. M., et al., 2011, *A&A*, **531**, A95
 Gehrels N., et al., 2004, *ApJ*, **611**, 1005
 Ghisellini G., Celotti A., 2001, *MNRAS*, **327**, 739
 Ghisellini G., Maraschi L., Treves A., 1985, *A&A*, **146**, 204
 Glaz J., Zhang Z., 2006, *Statistics & Probability Letters*, **76**, 1316
 Goldwurm A., et al., 2003, *A&A*, **411**, L223
 H. E. S. S. Collaboration et al., 2017, *A&A*, **600**, A89
 H. E. S. S. Collaboration et al., 2019, *MNRAS*, **486**, 3886
 Harrison F. A., et al., 2013, *ApJ*, **770**, 103
 Hartman R. C., et al., 1999, *ApJS*, **123**, 79
 Iacolina M. N., et al., 2019, The Astronomer’s Telegram, 12667, 1
 Krauss F., Becerra J., Carpenter B., Ojha R., Buson S., 2014, The Astronomer’s Telegram, 6361, 1
 Labanti C., et al., 2009, *Nuclear Instruments and Methods in Physics Research A*, **598**, 470
 Lidman C., Courbin F., Meylan G., Broadhurst T., Frye B., Welch W. J. W., 1999, *ApJ*, **514**, L57

Loru S., et al., 2019, *MNRAS*, **482**, 3857

Lovell J. E. J., Jauncey D. L., Reynolds J. E., Wieringa M. H., King E. A., Tzioumis A. K., McCulloch P. M., Edwards P. G., 1998, *ApJ*, **508**, L51

Lucarelli F., et al., 2019, The Astronomer’s Telegram, **12541**

Marcotulli L., et al., 2020, *ApJ*, **889**, 164

Mattox J. R., et al., 1996, *ApJ*, **461**, 396

Mattox J. R., Schachter J., Molnar L., Hartman R. C., Patnaik A. R., 1997, *ApJ*, **481**, 95

Melis A., et al., 2018, *Journal of Astronomical Instrumentation*, **7**, 1850004

Nair S., Jin C., Garrett M. A., 2005, *MNRAS*, **362**, 1157

Pacciani L., 2018, *A&A*, **615**, A56

Perotti F., Fiorini M., Incorvaia S., Mattaini E., Sant’Ambrogio E., 2006, *Nuclear Instruments and Methods in Physics Research A*, **556**, 228

Pittori C., 2013, *Nuclear Physics B Proceedings Supplements*, **239**, 104

Pittori C., The Agile-Ssdc Team, 2019, *Rendiconti Lincei. Scienze Fisiche e Naturali*, **30**, 217

Pittori C., et al., 2019a, The Astronomer’s Telegram, **12594**

Pittori C., et al., 2019b, The Astronomer’s Telegram, **12603**

Planck Collaboration et al., 2020, *A&A*, **641**, A6

Prest M., Barbiellini G., Bordignon G., Fedel G., Liello F., Longo F., Pontoni C., Vallazza E., 2003, *Nuclear Instruments and Methods in Physics Research A*, **501**, 280

Pushkarev A. B., Kovalev Y. Y., Lister M. L., 2010, *ApJ*, **722**, L7

Readhead A. C. S., Lawrence C. R., Myers S. T., Sargent W. L. W., Hardebeck H. E., Moffet A. T., 1989, *ApJ*, **346**, 566

Richards J. L., et al., 2011, *ApJS*, **194**, 29

Schlafly E. F., Finkbeiner D. P., 2011, *ApJ*, **737**, 103

Schleicher B., et al., 2019, *Galaxies*, **7**, 62

Stratta G., Capalbi M., Giommi P., Primavera R., Cutini S., Gasparri D., on behalf of the ASDC team 2011, preprint, ([arXiv:1103.0749](https://arxiv.org/abs/1103.0749))

Tavani M., et al., 2009, *A&A*, **502**, 995

Tavani M., Vittorini V., Cavaliere A., 2015, *ApJ*, **814**, 51

Tavecchio F., Maraschi L., Ghisellini G., 1998, *ApJ*, **509**, 608

Ubertini P., et al., 2003, *A&A*, **411**, L131

Vaughan S., Edelson R., Warwick R. S., Uttley P., 2003, *MNRAS*, **345**, 1271

Vercellone S., Romano P., 2014, in Proceedings of Swift: 10 Years of Discovery (SWIFT 10). p. 167, [doi:10.22323/1.233.0167](https://doi.org/10.22323/1.233.0167)

Vercellone S., et al., 2010, *ApJ*, **712**, 405

Vercellone S., et al., 2019, *A&A*, **621**, A82

Verrecchia F., et al., 2013, *A&A*, **558**, A137

Vitali F., et al., 2003, in Iye M., Moorwood A. F. M., eds, Society of Photo-Optical Instrumentation Engineers (SPIE) Conference Series Vol. 4841, Instrument Design and Performance for Optical/Infrared Ground-based Telescopes. pp 627–638, [doi:10.1117/12.459999](https://doi.org/10.1117/12.459999)

Vittorini V., et al., 2009, *ApJ*, **706**, 1433

Vittorini V., Tavani M., Cavaliere A., Striani E., Vercellone S., 2014, *ApJ*, **793**, 98

Vittorini V., Tavani M., Cavaliere A., 2017, *ApJ*, **843**, L23

Wiklund T., Combes F., 1996, *Nature*, **379**, 139

Wilms J., Buson S., Gokus A., Cheung T. C., Nowak M. A., Ciprini S., 2019, The Astronomer’s Telegram, **12737**, 1

Winkler C., 1994, *ApJS*, **92**, 327

Zerbi F. M., et al., 2004, in Moorwood A. F. M., Iye M., eds, Society of Photo-Optical Instrumentation Engineers (SPIE) Conference Series Vol. 5492, Ground-based Instrumentation for Astronomy. pp 1590–1601, [doi:10.1117/12.551145](https://doi.org/10.1117/12.551145)

APPENDIX A: GAMMA-RAY OBSERVATIONS

A1 AGILE data

The AGILE satellite (Tavani et al. 2009) is a mission of the Italian Space Agency (ASI) devoted to high-energy astrophysics. The AGILE scientific instrument combines four active detectors yielding broad-band coverage from hard X-ray to γ -ray energies: a Silicon

Table A1. AGILE-GRID fluxes and photon indices at different relevant epochs.

Time interval (MJD)	F($E > 100$ MeV) (photons $\text{cm}^{-2} \text{s}^{-1}$)	Photon index
58561.25 - 58563.25	$(8.1 \pm 1.2) \times 10^{-6}$	2.28 ± 0.17
58566.50 - 58568.50	$(6.5 \pm 1.1) \times 10^{-6}$	2.35 ± 0.20
58574.75 - 58576.75	$(1.2 \pm 0.1) \times 10^{-5}$	2.32 ± 0.15
58581.75 - 58583.75	$(1.4 \pm 0.2) \times 10^{-5}$	2.20 ± 0.14
58587.75 - 58589.75	$(1.7 \pm 0.2) \times 10^{-5}$	2.03 ± 0.16
58596.25 - 58598.25	$(2.2 \pm 0.2) \times 10^{-5}$	2.16 ± 0.13

Tracker (ST; Prest et al. 2003, 30 MeV–50 GeV), a co-aligned coded-mask hard X-ray imager, Super-AGILE (SA; Feroci et al. 2007, 18–60 keV), a non-imaging CsI Mini-Calorimeter (MCAL; Labanti et al. 2009, 0.3–100 MeV), and a segmented Anti-Coincidence System (ACS; Perotti et al. 2006). Any γ -ray detection is obtained by the combination of ST, MCAL and ACS; these three detectors form the AGILE Gamma-Ray Imaging Detector (GRID). A ground segment alert system allows the AGILE team to perform the full AGILE-GRID data reduction and the preliminary quick-look scientific analysis (Pittori 2013; Bulgarelli et al. 2014; Pittori & The Agile-Ssdc Team 2019).

PKS 1830–211 underwent an exceptionally bright active phase in γ -rays which started at the end of February 2019 and lasted approximately 2 months, as preliminarily reported in Lucarelli et al. (2019); Pittori et al. (2019a,b); Angioni (2019); Cardillo et al. (2019). We carried out the analysis of the AGILE-GRID consolidated data (archive ASDCSTDK) above 100 MeV with the new `Bui1d_25` scientific software, FM3.119 calibrated filter, H0025 response matrices. We applied South Atlantic Anomaly event cuts and 80° Earth albedo filtering. Only incoming γ -ray events with an off-axis angle lower than 60° were selected for the analysis. Statistical significance and flux determination of the point sources were calculated using the AGILE multi-source likelihood analysis software (MSLA; Bulgarelli et al. 2012) based on the Test Statistic (TS) method as formulated by Mattox et al. (1996). This statistical approach provides a detection significance assessment of a γ -ray source by comparing maximum-likelihood values of the null hypothesis (no source in the model) with the alternative hypothesis (point source in the field model).

We analyzed the γ -ray data above 100 MeV between February 16 and May 29, 2019 (MJD: 58530 - 58632). We analyzed 8 statistically independent light curves with a 48-hour time bin, with a MSLA approach by calculating the flux at the nominal position of the blazar. Each light curve is shifted by 6h with respect to the previous one, in order to better describe the time evolution of the γ -ray emission and preserving the photon statistics of a single 48h bin. In the multi-source analysis, we took into account the emission of the nearby sources within a radius of analysis of 10°. Position and fluxes of the field sources have been kept fixed at the values of the Second AGILE Catalog (Bulgarelli et al. 2019). The parameter quantifying the Galactic diffuse emission has been kept fixed at a standard value for an extra-galactic source. The parameter related to the isotropic diffuse emission has been kept free to vary. Figure A1 shows one of the eight independent light curves analyzed in our study, namely the one whose temporal bins are in agreement with the *Fermi*-LAT ones.

In Fig. A2 and Table A1, we present the AGILE-GRID photon index versus the $E > 100$ MeV flux, related to the main relative γ -

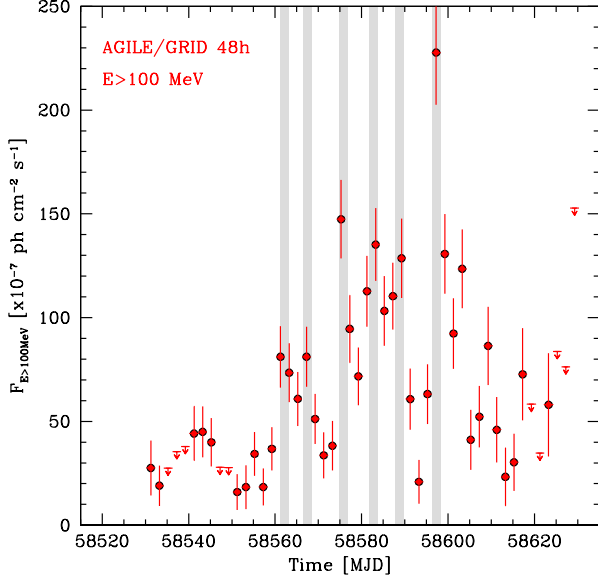


Figure A1. One of the 8 statistically independent AGILE-GRID 48h-bin light curves ($E > 100$ MeV) analyzed in our study, showing the maximum peak flux at $\text{MJD } 58597.25 \pm 1.0$. Grey vertical bands correspond to the six high activity levels reported in Table A1

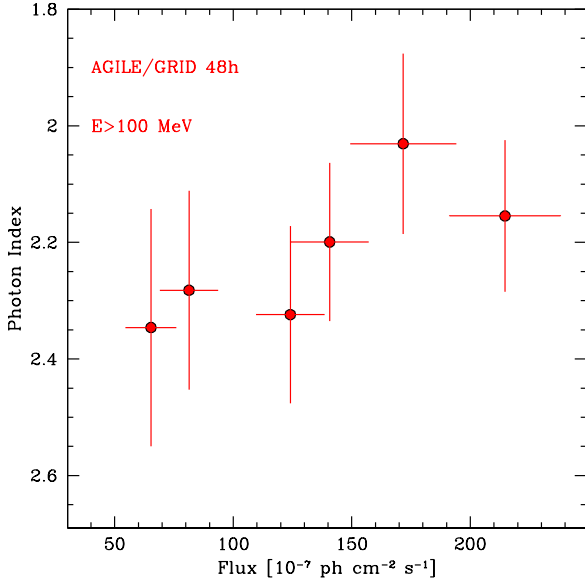


Figure A2. AGILE-GRID photon index versus the $E > 100$ MeV flux. See also Table A1.

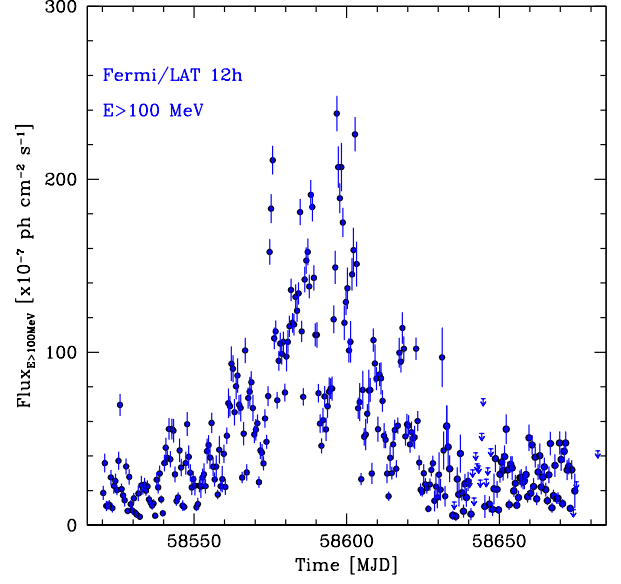


Figure A3. *Fermi*-LAT 12h-bin light curve obtained using likelihood standard analysis ($E > 100$ MeV) from 2019 February 06 to 2019 May 29.

ray peaks, emerging from the overall time evolution of the emission from the blazar (8 time-shifted light curves). The photon indices have been calculated with a binned analysis in the energy band 100 MeV - 3 GeV. Each flux has been calculated by keeping the correspondent spectral index fixed. No particular conclusions can be drawn on the correlation between the γ -ray flux and the photon index because of the too small number of data points (Spearman's coefficient $\rho = -0.89$, $p \approx 0.02$).

A2 *Fermi*-LAT data

We analyzed the *Fermi*-LAT (Atwood et al. 2009) data using the standard tools provided with the `ScienceTools` version v11r05p02, and the instrument response functions P8R3_SOURCE_V2 to produce light curves and spectra. We selected events within a region of 20° around the source nominal position, with reconstructed energy in the 0.1-300 GeV range. We filtered out γ -rays with zenith angles larger than 90° to reduce Earth limb γ -rays. We used the unbinned likelihood procedure to extract fluxes in energy and time bins. We modelled background using standard templates for isotropic and galactic diffuse background, and we included pointlike and diffuse sources from the fourth *Fermi*-LAT catalog (Abdollahi et al. 2020) inside the region of interest. Figure A3 and Figure A4 show the *Fermi*-LAT 12h-bin light curve obtained using likelihood standard analysis ($E > 100$ MeV) and the 12h-bin ($E > 300$ MeV) photon index versus 12h-bin flux, respectively. We note that the ($E > 300$ MeV) energy range used for the calculation of the spectral index is a conservative choice. The *Fermi*-LAT light-curves were calculated for both $E > 100$ MeV and $E > 300$ MeV, the former to allow a proper comparison with the AGILE-GRID one.

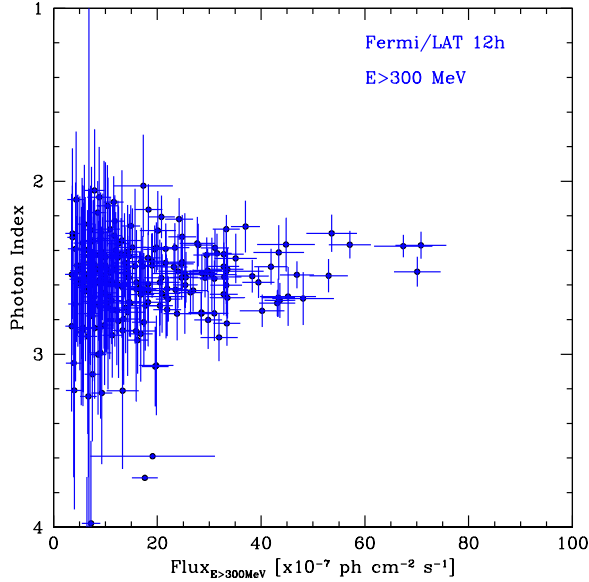


Figure A4. *Fermi*-LAT 12h-bin ($E > 300$ MeV) photon index versus 12h-bin flux from 2019 October 14 to 2019 May 20.

APPENDIX B: X-RAY OBSERVATIONS

Table B1 summarizes all the X-ray/hard X-ray observations, including *INTEGRAL*, *Swift*-XRT, *Chandra*, and *NuSTAR*.

B1 *INTEGRAL* data

The *INTEGRAL* (Winkler 1994) data set consists of a 180 ks public target of opportunity (ToO) observations performed from 03-April until 05-April 2019 plus 13 ks of public General Program, in which the source was in partially coded field of view, performed on 19-April-2019. The *INTEGRAL* data reduction of the low energy detector, ISGRI of γ -ray telescope IBIS (Ubertini et al. 2003) was performed using the standard Offline Scientific Analysis (OSA, Goldwurm et al. 2003) version 10.2 and the latest response matrices available. The source has been detected in the total ISGRI mosaic image (193 ks) at 7.1 and 7.2 sigma-level in the 15-30 keV and 30-200 keV energy ranges, respectively. The 20-50 keV ISGRI flux is 0.47 ± 0.07 counts s^{-1} (2.5×10^{-11} erg cm^{-2} s^{-1} or 4.4 mCrab). The 50-150 keV ISGRI flux is 0.55 ± 0.07 counts s^{-1} (7.9×10^{-11} erg cm^{-2} s^{-1} or 10 mCrab). The ISGRI 20-50 keV flux increased during the ToO observation by about 17% with respect to the averaged ISGRI flux reported in Donnarumma et al. (2011), while the 40-100 keV flux increment was of about 51%, which is consistent with a hardening of the source spectrum. We extracted the PKS 1830–211 ISGRI averaged spectrum (13-200 keV) using both the standard OSA spectral extraction and the alternative procedure to extract a faint source spectrum (see OSA user manual for details²). The resulting spectra were consistent. The best fit model consists in a simple power law with the photon index $\Gamma = 1.0 \pm 0.3$ and normalization $N_0 = 6.6^{+13}_{-2.1} \times 10^{-4}$ ph keV^{-1} cm^{-2} s^{-1} at 1 keV ($\chi^2_{red} = 1.0$; 4 d.o.f.).

² https://www.isdc.unige.ch/integral/download/osa/doc/11.1/osa_um_ibis.pdf

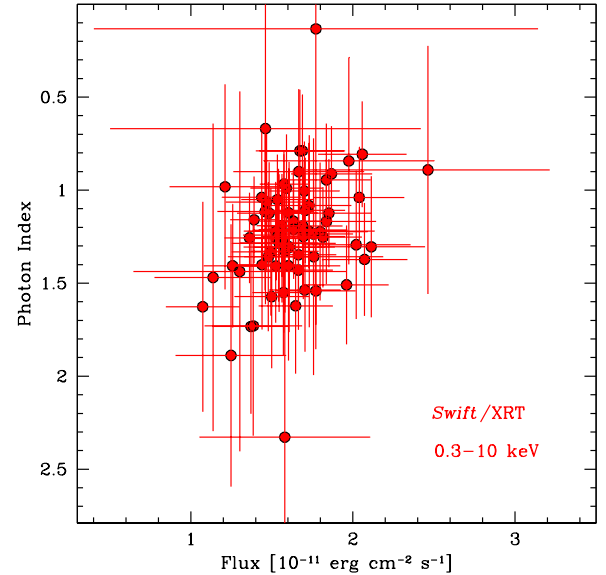


Figure B1. *Swift*/XRT photon index as a function of the 0.3-10 keV observed flux.

B2 *Swift*-XRT data

The *Neil Gehrels Swift* Observatory (*Swift* hereafter, Gehrels et al. 2004) data (Target ID 38422) were collected by activating two dedicated ToO observations triggered as a follow-up to *AGILE* detections. The X-ray Telescope (XRT, Burrows et al. 2005, on-board *Swift*) events files were processed using the XRTDAS software package (v.3.6.0) developed at SSC and distributed by the High Energy Astrophysics Science Archive Research Center (HEASARC) within the *HEASoft* package. Calibrated and cleaned event files were produced using the calibration files in the *Swift*-XRT CALDB 0(20200724) and standard filtering criteria with the *xrtpipeline* task. We used the *xrtproducts* task included in the XRTDAS package to extract the *Swift*-XRT source and background spectra using the appropriate response and ancillary files. We extracted spectra and light curves using circular apertures of radius $30''$, centered on the peak of the emission in the 0.3-10 keV data. Background spectra were extracted using source-free annular regions of the 80/120 pixel inner/outer radius.

Figure B1 shows the *Swift*/XRT photon index as function of the 0.3-10 keV observed flux. A possible harder-when-brighter trend is present (Spearman's coefficient $\rho = -0.31$, $p < 0.009$).

B3 *Chandra* data

Chandra (Winkler 1994) pointed at PKS 1830–211 on discretionary director time (DDT) observations. Five observations were acquired, three in April and May 2019 and two in June 2019. Table B2 shows the log of the *Chandra* observations. We reprocessed the *Chandra* data using the “*Chandra* Interactive Analysis of Observations” (CIAO) package. For each observation, we created the clean level-2 event file using the *chandra_repro* script. De Rosa et al. (2005) reported that *Chandra* can resolve the two lensed images of PKS 1830–211 at an angular distance of the order of $1''$. In order to search for possible

Table B1. Log of X-ray observations. MJDs are rounded for sake of simplicity. Actual MJD values can be derived from the ID column.

Date (MJD)	Satellite	ID	duration (ks)
58545	Swift-XRT	00038422035	2.0
58548	Swift-XRT	00038422036	2.0
58550	<i>NuSTAR</i>	804606280002	40
58551	Swift-XRT	00038422037	1.9
58554	Swift-XRT	00038422038	2.0
58558	Swift-XRT	00038422039	1.9
58560	Swift-XRT	00038422040	1.7
58563	Swift-XRT	00038422041	2.1
58566	Swift-XRT	00038422042	2.0
58567	Swift-XRT	00038422044	1.8
58568	Swift-XRT	00038422045	2.0
58572	Swift-XRT	00038422047	1.8
58576	Swift-XRT	00038422049	0.8
58576	INTEGRAL (17 SCW)	16700030001	–
58577	INTEGRAL (15 SCW)	16700030001	–
58578	Swift-XRT	00038422050	1.6
58578	INTEGRAL (9 SCW)	16700030001	–
58581	Swift-XRT	00038422051	2.0
58583	Swift-XRT	00038422053	1.6
58584	Swift-XRT	00038422054	2.2
58585	Swift-XRT	00038422055	1.6
58587	Swift-XRT	00038422056	2.0
58590	Swift-XRT	00038422057	1.9
58592	Chandra	22197	15
58592	INTEGRAL (6 SCW)	16200150003	–
58593	Swift-XRT	00038422058	1.9
58600	Swift-XRT	00038422059	0.01
58602	Swift-XRT	00038422060	1.5
58602	Swift-XRT	00038422061	0.4
58606	Swift-XRT	00038422062	2.3
58608	INTEGRAL (1 SCW)	16200150003	–
56609	Swift-XRT	00038422063	2.0
58610	Chandra	22198	20
58615	Swift-XRT	00038422064	2.6
58618	Swift-XRT	00038422065	2.9
58621	Swift-XRT	00038422066	2.3
58627	Swift-XRT	00038422067	2.9
58627	Chandra	22199	25
58630	Swift-XRT	00038422068	2.6
58633	Swift-XRT	00038422069	1.4
58636	Swift-XRT	00038422070	3.3
58639	Swift-XRT	00038422071	0.2
58642	Swift-XRT	00038422072	2.7
58645	Swift-XRT	00038422073	2.2
58649	Chandra	22239	10
58650	Chandra	22240	10
58654	Swift-XRT	00038422074	1.5
58658	Swift-XRT	00038422075	0.3
58660	Swift-XRT	00038422076	1.1
58665	Swift-XRT	00038422077	1.1

spectral differences of the two hotspots (see below), we first align the WCS grid of all observations to the same reference coordinate. We follow the standard CIAO thread for absolute astrometric correction. For all observations, we use the `wcs_match` tool to compute the offset between the observed centroid and the reference coordinates. Hence, this can be input in `wcs_update` script to update the WCS grid of all the event files to match the reference coordinates (i.e. the coordinates of the source as observed in the first observation).

For all observations, we extracted the spectrum of PKS 1830–211

from a circular region with a radius of $4''$. We took the background from an annular region, centered on the source, and with inner and outer radii of $20''$ and $25''$, respectively. We fitted the spectra using XSpec v12. It was already reported that PKS 1830–211 displays a highly absorbed spectrum, with the absorption arising in the intervening lensing galaxy at $z=0.89$. Thus, we fitted all the spectra with a model that included the Galactic absorption ($N_{\text{H}}^{\text{gal}} = 2.19 \times 10^{21} \text{ cm}^{-2}$, [Dickey & Lockman 1990](#)), the absorption at the redshift of the lensing galaxy, and a power law continuum. The free parameters of

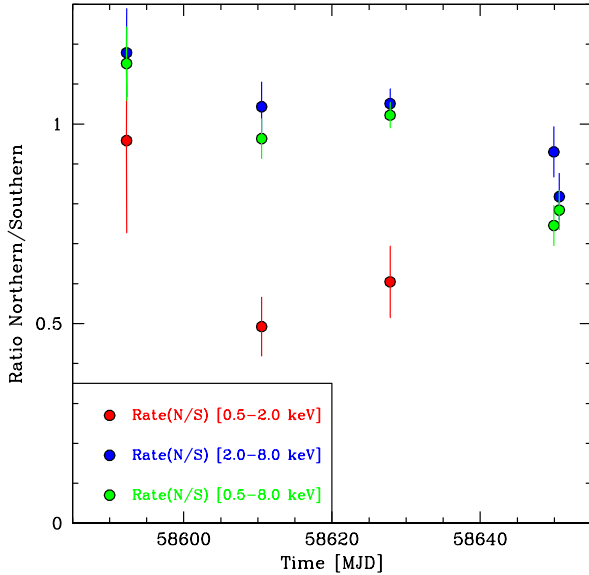


Figure B2. Ratios between the count-rate measured in the north and south hotspot of PKS 1830–211 as a function of time in the 0.5–2.0 (red), 2.0–8.0 (blue) and 0.5–8.0 keV (green) energy range.

Table B2. *Chandra* observation log

Obs. ID	Date dd/mm/yyyy	Duration ^a	Observed Flux ^b	
			$F_{0.5-2.0\text{keV}}$	$F_{2.0-10.0\text{keV}}$
22197	19/04/2019	15	0.11 ± 0.03	1.3 ± 0.4
22198	07/05/2019	20	0.15 ± 0.03	1.6 ± 0.3
22199	24/05/2019	25	0.11 ± 0.02	1.3 ± 0.2
22239	15/06/2019	10	0.12 ± 0.03	1.4 ± 0.3
22240	16/06/2019	10	0.12 ± 0.03	1.4 ± 0.3

^a Total duration of the observation in ksec.

^b Observed flux in the quoted bands. Units of $10^{-11} \text{ erg s}^{-1} \text{ cm}^{-2}$.

the fits are the intervening column density, $N_{\text{H}}^{\text{lens}}$, the photon index, and the normalization of the power law. Figure B3 shows the time evolution of the free parameters of our fits, observation by observation, while the observed fluxes measured from our spectral fitting are reported in Table B2. In all the *Chandra* observations, the global X-ray spectrum of PKS 1830–211 remained substantially stable, both in flux and in spectral shape.

B4 *NuSTAR* data

NuSTAR (Harrison et al. 2013) consists of two focal plane modules, FPMA and FPMB, is sensitive at 3–78.4 keV and has a field-of-view of $10'$ at 10 keV (Harrison et al. 2013). *NuSTAR* has a $18''$ FWHM with a half-power diameter of $58''$. We analyzed the *NuSTAR* observation of PKS 1830–211 performed in March 2019. The observation log is given in Table B3.

The raw events files were processed using the *NuSTAR* Data

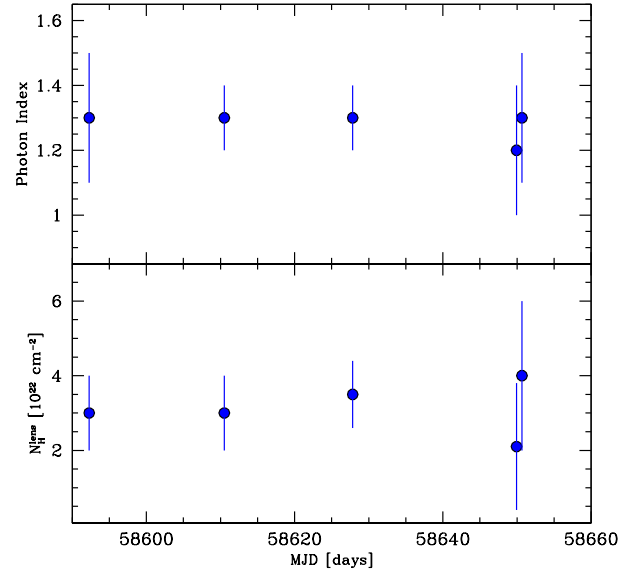


Figure B3. Time evolution of the parameters of the *Chandra* spectra. Upper panel: Photon index. Lower panel: Absorbing column density at the redshift of the lensing galaxy.

Analysis Software package v. 2.0.0. NuSTARDAS³. Calibrated and cleaned event files were produced using the calibration files in the *NuSTAR* CALDB (20200813) and standard filtering criteria with the nupipeline task. We used nuproducts task included in the NuSTARDAS package to extract the *NuSTAR* source and background spectra using the appropriate response and ancillary files. We extracted spectra and light curves in each focal plane module (FPMA and FPMB) using circular apertures of radius $90''$, corresponding to $\sim 90\%$ of the encircled energy, centered on the peak of the emission in the 3–78.4 keV data. Background spectra were extracted using source-free regions on the same detector as the source. As shown in Table B3, the background count rates are a small fraction ($\sim 6\%$) of the source count rates. The spectra were binned to have at least 30 counts per bin.

APPENDIX C: IR-OPTICAL-UV OBSERVATIONS

C1 *Swift*/UVOT data

The *Swift*/UVOT data were accumulated during the whole observing campaign, in order to establish the most reliable upper limits in the v , b , u , $w1$, $m2$, and $w2$ filters. Data were processed with HEASOFT v6.23 and CALDB (20201026). Due to the crowded field, particularly in optical bands, some nearby stars could contaminate an aperture of standard radius (see Figure C1). To extract source counts we used a non-standard aperture of radius equal to the PSF FWHM, $2.2''$, and three uncontaminated circular regions for the background extraction. We extracted source fluxes in each filter image available in each observation and on the sum of all the available images during the 2019 flaring campaign in each filter. No detections were obtained in any

³ http://heasarc.gsfc.nasa.gov/docs/nustar/analysis/nustar_swguide.pdf

Table B3. *NuSTAR* observation log.

Observation ID ^a	RA_PNT ^b (deg.)	DEC_PNT ^c (deg.)	Exposure ^d (ksec)	Start Date ^e	rate ^f (cts/s)	background ^g
80460628002	278.4356	-21.0336	41.4	2019-03-08T20:21:09	0.458±0.004	~6%

Notes: ^aObservation identification number; ^bRight Ascension of the pointing; ^cDeclination of the pointing; ^d total net exposure time; ^e start date and time of the observation; ^f mean value of the net count rate in the circular source extraction region with 90'' radius in the energy range 3–78.4 keV; ^g background percentage in the circular source extraction region with 90'' radius and in the energy range 3–78.4 keV.

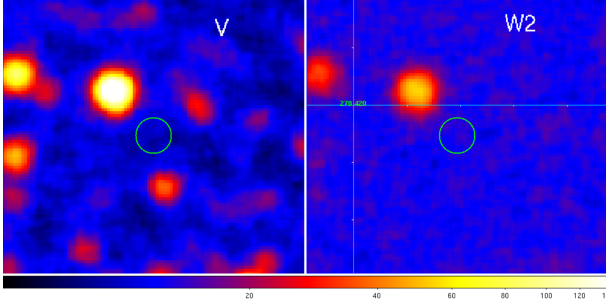

Figure C1. UVOT image for the V (left) and W2 filters. The non-standard aperture of size 2.2'' is shown in cyan color.

Table C1. *Swift*/UVOT data.

Filter	Upper limits (dereddened) (erg s ⁻¹ cm ⁻²)
<i>v</i>	< 1.80 × 10 ⁻¹³
<i>b</i>	< 8.96 × 10 ⁻¹⁴
<i>u</i>	< 2.42 × 10 ⁻¹⁴
<i>w1</i>	< 1.74 × 10 ⁻¹⁴
<i>m2</i>	< 1.29 × 10 ⁻¹⁴
<i>w2</i>	< 1.45 × 10 ⁻¹⁴

band, so we could not confirm the detection reported in [Abhir et al. \(2021\)](#). Observed magnitudes were converted into dereddened fluxes according to the CALDB conversion factors ([Breeveld et al. 2011](#)) and a mean Galactic extinction law ([Fitzpatrick 1999](#)) and E(B-V) value of 0.397 ([Schlafly & Finkbeiner 2011](#)). Flux ULs on the summed images are reported in Table C1.

C2 REM data

The infrared J, H, and K data have been obtained with the REMIR camera ([Vitali et al. 2003](#)), at the focal plane of the REM telescope ([Zerbi et al. 2004](#)), in the ESO La Silla (Chile) observatory. Observations were carried out in 23 nights, in March and April 2019, of which 12 were photometric. The NIR frames have been reduced with the semi-automatic pipeline Riace ([Giannini et al. in preparation](#)), which performs the frames stack (to produce the science and sky frames), then uses the 2MASS stars in the field to calibrate the aperture photometry of the science target. Figure 3 panel (b) shows the REM light-curves for the H and K filters. Data are reported in Table C2.

Table C2. REM IR data.

Time (MJD)	H-filter (dereddened) (erg s ⁻¹ cm ⁻²)	K-filter (dereddened) (erg s ⁻¹ cm ⁻²)
58565.0	1.64 × 10 ⁻¹³ ± 6.19 × 10 ⁻¹⁴	–
58566.0	1.98 × 10 ⁻¹³ ± 7.45 × 10 ⁻¹⁴	2.54 × 10 ⁻¹³ ± 9.57 × 10 ⁻¹⁴
58571.0	2.17 × 10 ⁻¹³ ± 1.03 × 10 ⁻¹³	2.32 × 10 ⁻¹³ ± 8.73 × 10 ⁻¹⁴
58573.0	2.38 × 10 ⁻¹³ ± 6.65 × 10 ⁻¹⁴	2.79 × 10 ⁻¹³ ± 1.05 × 10 ⁻¹³
58574.0	2.17 × 10 ⁻¹³ ± 8.16 × 10 ⁻¹⁴	2.54 × 10 ⁻¹³ ± 7.11 × 10 ⁻¹⁴
58577.0	–	3.05 × 10 ⁻¹³ ± 5.66 × 10 ⁻¹⁴
58578.0	2.17 × 10 ⁻¹³ ± 6.06 × 10 ⁻¹⁴	2.79 × 10 ⁻¹³ ± 5.16 × 10 ⁻¹⁴
58580.0	2.38 × 10 ⁻¹³ ± 6.65 × 10 ⁻¹⁴	2.54 × 10 ⁻¹³ ± 4.71 × 10 ⁻¹⁴
58584.0	1.50 × 10 ⁻¹³ ± 5.65 × 10 ⁻¹⁴	1.46 × 10 ⁻¹³ ± 4.09 × 10 ⁻¹⁴
58585.0	1.80 × 10 ⁻¹³ ± 5.04 × 10 ⁻¹⁴	1.93 × 10 ⁻¹³ ± 5.39 × 10 ⁻¹⁴
58586.0	–	1.93 × 10 ⁻¹³ ± 5.39 × 10 ⁻¹⁴

APPENDIX D: RADIO OBSERVATIONS

D1 SRT/Medicina data

A radio observation campaign was undertaken with two INAF radio telescopes: the Sardinia Radio Telescope⁴ (SRT) and the Medicina radio telescope⁵. The radio follow-up started on MJD 58590.2 and ended on MJD 58662.9. 18 dual-frequency observing sessions were performed: 8 with Medicina at 8.3 and 25.4 GHz using total power back-end with 250 and 680 MHz bandwidth, respectively, and 10 sessions with the SRT at 7 and 25.5 GHz, where SARDARA back-end ([Melis et al. 2018](#)) was used with a 1400 MHz bandwidth. Single-dish radio mapping techniques were exploited to perform On The Fly maps of the source and a sample of the best-known radio astronomical flux calibrators (3C 286, 3C 295 and NGC 7027). The follow-up was undertaken in the context of two INAF ToO programs and one Director Discretionary Time proposal. Preliminary results were published in [Iacolina et al. \(2019\)](#). Radio imaging data analysis and calibration were performed using the techniques explained in [Egron et al. \(2017b,a\)](#) and [Loru et al. \(2019\)](#), comparing counts of the Gaussian fit in the target image with calibrators images and cross-scans. Most of the radio data were of good quality. However, the low elevation of the source, bad weather (fog and rain) and strong radio frequency interference (RFI) affected the data scans (i.e. enhanced and variable error bars in flux densities). Figure 3, panel (a), shows the multi-frequency radio flux density light-curve (in Jy) obtained with SRT and Medicina radio telescopes in the MJD 58590.2–58662.9 period.

⁴ <http://www.srt.inaf.it/>

⁵ <http://www.med.ira.inaf.it/>

Table D1. SRT and Medicina radio data.

SRT times and data		
Time (MJD)	7 GHz (Jy)	25.5 GHz (Jy)
58596.253	15.8 ± 1.0	11.9 ± 0.8
58599.193	15.2 ± 1.0	11.7 ± 1.0
58601.226	14.5 ± 0.8	11.7 ± 1.5
58604.208	14.6 ± 0.9	11.5 ± 1.5
58607.184	14.0 ± 0.9	11.2 ± 1.0
58610.191	14.6 ± 0.8	11.3 ± 0.8
58613.190	15.2 ± 0.8	11.9 ± 1.3
58617.147	14.9 ± 1.0	11.6 ± 1.0
58626.113	15.4 ± 1.5	11.5 ± 0.5
58630.169	15.7 ± 1.0	10.5 ± 1.0

Medicina times and data		
Time (MJD)	8.3 GHz (Jy)	25.5 GHz (Jy)
58590.228	16.0 ± 1.0	9.8 ± 0.9
58592.236	17.0 ± 1.0	11.8 ± 0.5
58644.900	16.0 ± 1.0	10.2 ± 0.5
58649.941	17.0 ± 0.5	10.7 ± 0.5
58651.925	17.0 ± 0.7	10.7 ± 0.9
58655.902	16.5 ± 0.4	9.7 ± 0.6
58659.902	17.1 ± 0.4	9.8 ± 0.6
58662.905	17.6 ± 0.5	10.7 ± 1.0

D2 OVRO data

The Owens Valley Radio Observatory (OVRO) 40-Meter Telescope uses off-axis dual-beam optics and a cryogenic receiver with 2 GHz equivalent noise bandwidth centered at 15 GHz. Gain fluctuations, atmospheric and ground contributions are removed with the double switching technique (Readhead et al. 1989) where the observations are conducted in an ON-ON fashion such that one of the beams is always pointed on the source. The two beams were rapidly alternated using a Dicke switch until May 2014. In May 2014 a new pseudo-correlation receiver with a 180 degree phase switch replaced the old receiver. To compensate for gain drifts relative calibration is obtained with a temperature-stable noise diode. The primary flux density calibrator is 3C 286 with an assumed value of 3.44 Jy (Baars et al. 1977), DR21 is used as secondary calibrator source. Richards et al. (2011) gives details about the observation procedure and data reduction. Figure 3, panel (a), shows the OVRO radio flux density light-curve (in Jy).

This paper has been typeset from a \LaTeX file prepared by the author.